A *post mortem* 3-D Brain Hemisphere Cortical Tau and Amyloid–β Pathology Mapping and Quantification as a Validation Method of Neuropathology Imaging

Lojze M. Smid[1,2], **Vladimir Kepe**[1], **Harry V. Vinters**[1], **Mara Bresjanac**[2], **Tatsushi Toyokuni**[1], **N. Satyamurthy**[1], **Koon-Pong Wong**[1], **Sung-Cheng Huang**[1], **Daniel H.S. Silverman**[1], **Karen Miller**[1], **Gary W. Small**[1], and **Jorge R. Barrio**[1,*]

[1]David Geffen School of Medicine at UCLA, Los Angeles, CA

[2]School of Medicine, University of Ljubljana, Ljubljana, Slovenia

Abstract

This work is aimed at correlating *pre mortem* [F-18]FDDNP PET scan results in a patient with dementia with Lewy bodies (DLB), with cortical neuropathology distribution determined *post mortem* in three physical dimensions in whole brain coronal sections. Analysis of total Aβ distribution in frontal cortex and posterior cingulate gyrus confirmed its statistically significant correlation with cortical [F-18]FDDNP PET binding values (distribution volume ratios, DVR) ($p<0.001$, R=0.97, R^2=0.94). Neurofibrillary tangle (NFT) distribution correlated significantly with cortical [F-18]FDDNP PET DVR in the temporal lobe ($p<0.001$, R=0.87, R^2=0.76). Linear combination of Aβ and NFT densities was highly predictive of [F-18]FDDNP-PET DVR through all analyzed regions of interest ($p<0.0001$, R=0.92, R^2=0.85), and both densities contributed significantly to the model. Lewy bodies (LB) were present at a much lower level than either Aβ or NFTs and did not significantly contribute to the *in vivo* signal. [F-18]FDG PET scan results in this patient were consistent with the distinctive DLB pattern of hypometabolism. This work offers a mapping brain model applicable to all imaging probes for verification of imaging results with Aβ and/or tau neuropathology brain distribution using immunohistochemistry, fluorescence microscopy and autoradiography.

Keywords

[F-18]FDDNP; dementia with Lewy bodies; brain pathology mapping; amyloid and tau immunocytochemistry

Introduction

Neuroimaging of dementia, particularly using positron emission tomography (PET) with small molecular imaging probes targeting amyloid-like brain deposits, has been an active area of research aiming at early diagnosis and *non-invasive* evaluation of disease progression. 2-(1-{6-[(2-[F-18]Fluoroethyl)(methyl)amino]-2-naphthyl}ethylidene)malononitrile ([F-18]-FDDNP) was the first imaging probe successfully used for *in vivo* imaging of AD-related pathology in humans [1]. Because of its *in vitro* affinity for β-amyloid (Aβ) fibrils, as initially shown by fluorescence and

*To whom correspondence should be addressed: Jorge R. Barrio, PhD, David Geffen School of Medicine at UCLA, Department of Molecular and Medical Pharmacology, CHS B2-086A, 694817, 10833 Le Conte Avenue, Los Angeles, CA 90095-6948. jbarrio@mednet.ucla.edu.

radioactive assays [2], unlabeled FDDNP has been used as an *in vitro* fluorescent dye with fluorescence microscopy for labeling amyloid-like protein deposits containing β-pleated sheet aggregates in the histological brain sections of neurodegenerative disorders associated with Alzheimer disease (AD) [2, 3], variant and sporadic Creutzfeldt-Jakob disease (CJD), as well as in a prion protein gene mutation-associated Gerstmann-Sträussler-Scheinker syndrome (GSS) [4], Lewy bodies (LB) in dementia with Lewy bodies (DLB), progressive supranuclear palsy (PSP) and Parkinson's disease (PD) [3]. [F-18]FDDNP-PET successfully differentiates clinically defined AD patients and mild cognitive impairment (MCI) patients from cognitively normal subjects with higher specificity and sensitivity than either [F-18]FDG-PET or structural MR imaging [5]. *In vitro* FDDNP labeling properties in histological brain sections in sporadic CJD, variant CJD and GSS has also led to the use of [F-18]FDDNP-PET as the first successful method for visualization and quantification of prion protein amyloid deposits in the living brain of patients [6–8].

The regional brain distribution of [F-18]FDDNP PET signal in patients with AD agrees well with known AD-related pathology distribution and also agrees with the neuropathological criteria for Alzheimer's disease diagnosis [9–11] as shown by *post mortem* pathological determinations in the brain of an AD patient previously scanned [5, 12]. However the same detailed work in other dementias has not yet been performed with [F-18]FDDNP PET.

In this report we present the new approach for validation of *in vivo* PET cortical binding pattern with *post mortem* mapping of Aβ and tau pathology on coronally cut brain tissue from one hemisphere at five levels, an approach similar to the method for Braak staging of tau pathology [13]. To demonstrate the effectiveness of this method we applied it to the validation of [F-18]FDDNP PET scans of a subject with confirmed DLB. Since this method provides an opportunity for mapping the whole brain with quantitation of pathology load, it is suitable for similar analysis of various neurodegenerative diseases. This method is particularly valuable because it also permits for the first time identification and mapping of tau aggregates with brain PET imaging and correlation of these results with *post mortem* histopathological findings.

Recent work from our laboratory [14] with a homozygous triple-transgenic rat model of AD (Tg478/Tg1116/Tg11587), originally derived by Flood and colleagues [15], as well as previous work from others [16], indicates that Aβ brain accumulation in this transgenic model of AD manifests primarily as diffuse, rather that cored fibrillar plaques. The robust age-associated *in vivo* [F-18]FDDNP binding seen in the brain of these animals – as well as the correlation of *in vivo* [F-18]FDDNP binding with Aβ content – corroborates that [F-18]FDDNP labels both diffuse and fibrillar Aβ plaques typically present in DLB [17] and provides further justification for its use in this work.

Patient history

A 73-year old Caucasian man, a retired university professor with 19 years of education, was evaluated for worsening memory problems as part of a prospective University of California, Los Angeles dementia neuroimaging project. Written informed consent was obtained from the patient at the time of scanning in the presence of his wife, in accordance with procedures of the Human Subjects Protection Committee of the University of California, Los Angeles and the study was performed under standard ethics guidelines. Due to the presence of metal in his body, this patient was not a candidate for a brain MRI scan. For brain anatomical correlations of PET imaging data and assessment of brain atrophy, the patient received instead a CT scan. He and his wife described a four-year history of difficulties giving lectures and organizing information. They also noted intermittent visual hallucinations that improved with the use of low-dose atypical antipsychotic medications as needed. The patient

was also taking donepezil (5 mg), ginkgo biloba, and vitamin E (400 IU) daily for his memory complaints. He did not report problems sleeping through the night. Physical examination indicated evidence of Parkinsonian symptoms, including slight loss of expression, diction and volume of speech, minimal hypomimia, a slight and infrequent tremor at rest and with action, and minimal body bradykinesia. His activity of daily living assessment indicated some difficulty tying his shoes, as well as occasional urinary incontinence.

Despite his high baseline intellectual functioning and academic achievements, cognitive impairment was noted on examination. Neuropsychological evaluation included a Mini–Mental State Examination [18] and a battery of neuropsychological tests [19] that assessed five cognitive domains: memory (Wechsler Memory Scale Logical Memory Test and Verbal Paired Associations II, Buschke–Fuld for Selective Reminding Test [Total Recall], and Rey-Osterreich Complex Figure Recall Test [Delayed Recall]), language (Boston Naming Test, Letter Fluency Test and Animal Naming Test), attention and speed of information processing (Trail Making Test A, Stroop Color Test [Kaplan version], and Digit Symbol Test, Wechsler Adult Intelligence Scale [WAIS]), executive functioning (Trail Making Test B, Stroop interference [Kaplan version], and Wisconsin Card Sorting Test, Perseverative Errors), and visuospatial functioning (WAIS Block Design Test, Rey–Osterreich Complex Figure Test [copy], and Benton Visual Retention Test). Attention, concentration, abstract reasoning, and delayed verbal recall were intact, but impairments were observed in immediate and delayed recall of a rote earned list, and immediate recall for simple designs and a complex figure. The patient also showed impairment in semantic and phonemic fluency and visual spatial abilities. No evidence of psychosis or depression was observed.

Methods

[F-18]FDDNP was synthesized as previously described [20] and PET scans were performed with the ECAT HR scanner (Siemens CTI). Dynamic [F-18]FDDNP PET scan was obtained for 2 hours after a bolus injection and [F-18]FDG PET scan was acquired for 1 hour after bolus injection. Scans were corrected for radioactive decay and reconstructed with the use of filtered back-projection (Hann filter, 5.5 mm full width at half maximum), with correction for scatter and measured attenuation [21]. Movement correction of the [F-18]FDDNP PET images was performed as described previously [22]. Quantification of the data on [F-18]FDDNP binding was performed using the Logan graphic method with cerebellum as the reference region [23, 24] on the movement corrected PET images and [F-18]FDDNP distribution volume ratio (DVR) images were created. The slope of the linear portion of the Logan plot is equal to the distribution volume of the probe in a region of interest (ROI) divided by the distribution volume in the reference region. Brain boundaries for registration were obtained with the [F-18]FDDNP image obtained over the first 5 min of the scan and representing the perfusion image.

Quantification of [F-18]FDG-PET scans was performed on summed brain images (within 30 to 60 minutes after [F-18]FDG injection) and was expressed as the relative standardized uptake value (SUVR) with reference to the cortical white matter. Both, parametric [F-18]FDDNP and summed [F-18]FDG PET images were co-registered to the CT image for further analysis. Average [F-18]FDDNP binding values and [F-18]FDG standardized uptake value ratios (SUVR) were calculated for chosen regions of interest (ROI) for each PET probe separately using Amide software [25].

The patient died at his home 46 months after PET scanning. Consent from the closest living relative – upon donation of the patient's brain to the UCLA brain bank (H.V. Vinters, UCLA Department of Pathology) – was obtained for further histopathological

determinations. After autopsy, the brain was fixed in 10% buffered formalin, each hemisphere sectioned into 1.5 cm thick coronal sections and divided in up to four smaller blocks prior to freezing and cryosectioning into 40 μm thick sections. Each coronal cross-section through the whole hemisphere was thus represented by up to four separate tissue sections.

Whole hemisphere autoradiography was performed as described previously [2, 26]. Briefly, free-floating brain tissue sections were dehydrated, de-fattened in xylene at 60 °C for 3 hours, rehydrated and mounted on glass slides. Each tissue piece was then incubated for 25 minutes in solution of 3.7 MBq of [F-18]FDDNP in 10 ml of 1% ethanol in water. Sections were differentiated by washing with 60% 2-methyl-2-butanol (Sigma, St. Louis, MO, USA) at 25 °C for 90 seconds, exposed to the phosphoimaging plates and analyzed using FUJI BAS 5000 Phosphorimager (Fuji Film Medical Systems, USA).

FDDNP Fluorescence Histochemistry was also performed as described previously [3]. Briefly, free floating tissue sections were de-fattened, rehydrated and incubated in 10 μM FDDNP in 1% ethanol solution for 10 minutes, rinsed, mounted and covered using aqueous mounting medium (Vectashield, Vector laboratories, Burlingame, CA). As a standard method for dementia-associated pathology detection, Thioflavin S fluorescence histochemistry was performed on free-floating sections using 0.05% Thioflavin S (Sigma, St. Louis, MO, USA) solution in 50% ethanol, followed by differentiation in 70% ethanol for 30 seconds. Sections were then rinsed, mounted and covered using aqueous mounting medium (Vectashield, Vector laboratories, Burlingame, CA).

Pathology Distribution on Whole-hemisphere Coronal Tissue Sections by Immunohistochemistry (IHC) was performed on free-floating sections for detection of Aβ, tau and α-synuclein tissue deposits. Epitope retrieval was carried out with pre-treatment in 85% formic acid for 5 minutes for Aβ and α-synuclein IHC, no formic acid pretreatment was used for hyperphosphorylated tau IHC. Aβ IHC detection was done using mouse monoclonal antibody 6F/3D (Dako, Carpinteria, CA). Sections were then rinsed in buffer, before a 5% normal horse serum was applied for 30 min to block the nonspecific binding of the secondary antibody. Incubation with the primary antibody (1:100) was performed overnight at 24°C. Incubation in the biotinylated horse anti-mouse secondary antibody (1:200; Vector Laboratories, Burlingame, CA) was followed by incubation in the avidin-biotin-peroxidase complex (ABC Standard Elite Kit; Vector Laboratories) and chromogen (3',3-diaminobenzidine; Sigma, St. Louis, MO, USA) solution. Hyperphosphorylated tau IHC detection was performed with mouse monoclonal antibody AT8 (Innogenetics, Belgium, 1:1000, 2hrs at 24°C) and α-synuclein detection was performed using LB509 mouse monoclonal antibody (Zymed Laboratories, San Francisco, CA, 1:100, 2 hrs at 24°C). In both cases blocking and detection steps were identical to those described for Aβ IHC.

Co-localization Analysis

In vitro Measures: FDDNP Fluorescence Histochemistry and Immunofluorescence (IF)—For interpretation of radioactivity accumulation in the [F-18]FDDNP PET-scanned patient brain, co-localization microscopy analysis of FDDNP labeling (fluorescence histochemistry) and immunofluorescence (IF) detection of Aβ, hyperphosphorylated tau or α-synuclein in brain specimens was performed. Sets of three consecutive 5-μm brain tissue sections (one section for each deposited protein IF analysis), were cut from paraffin embedded tissue blocks from eight representative cortical and subcortical brain regions. After deparaffination, tissue autofluorescence was quenched by incubation in 0.05% $KMnO_4$ for 5 minutes [27] and then FDDNP histochemistry was performed as described above. Photomicrographs of FDDNP labeled structures were taken

using a Nikon Eclipse E600 fluorescence microscope (filter: EX 465–695, DM 505, BA 515–555), and their coordinates were recorded. IF labeling was performed on the same tissue pieces after pretreatment with 85% formic acid for 5 minutes. IF experiments for specific pathology were performed with the following antibodies: anti-Aβ mouse monoclonal antibody 6F/3D (1:50; Dako, Carpinteria, CA); anti-hyperphosphorylated tau mouse monoclonal antibody AT8 (1:250; Pierce Endogen, Rockford, IL); anti-α-synuclein sheep polyclonal antibodies (1:80; AB5334P, Chemicon, Temecula, CA). In each case overnight primary antibody incubation (at 10°C) was followed by biotinylated secondary antibody (1:1000, 90 minutes; Vector Laboratories, Burlingame, CA) and Alexa Fluor 546 streptavidin conjugate (1:750, 90 minutes; Invitrogen, Karlsruhe, Germany) incubations. Photomicrographs were taken at previously recorded coordinates (filter: EX 528–553, DM 565, BA 590–650) and image pairs were analyzed using custom made software (mImage, developed by G. Repovš [6]. Gaussian smoothing filter was applied to images to eliminate local noise and optimal thresholds for FDDNP and IF image signal segmentation were determined. For each FDDNP–labeled structure, co-localization coefficients (m1 and m2) [28] were computed to quantify the proportion of the two signals inside the co-localized area.

Correlation of [F-18]FDDNP PET with *In vitro* Measures—[F-18]FDDNP PET and immunohistology correlation analysis was performed after high-resolution digitalization of anti-Aβ and anti-tau immunostained coronal sections. Five coronal cross-sections, composed of 12 tissue sections were manually co-registered to CT brain image using anatomical landmarks and twenty one small regions of interest (ROI) were selected for analysis: nine regions of frontal cortex (on four different coronal sections), two regions of primary sensorimotor cortex, region of posterior cingulate gyrus, five regions of temporal cortex (on two coronal sections), two medial temporal lobe regions (including hippocampus, on two coronal sections) and two regions of occipital cortex (Table 1; Figure 2).

The optical densities of IHC ROI were calculated using Image J software (US National Institutes of Health, Bethesda, MD). Segmentation of digitized IHC images for IHC labeling identification was performed using standardized threshold levels, calculated form average white matter optical density values for each analyzed section. The method resulted in less than 0.5% above-threshold cortical area in negative control IHC sections.

Statistical Analysis—Pearson's correlation coefficients (R) and coefficients of determination (R^2) were calculated for correlation between [F-18]FDG PET SUVRs or [F-18]FDDNP PET DVRs and Aβ or tau deposit density, depending on the predominant deposit type in the analyzed region, as well as with α-synuclein, where present. Multiple linear regression analyses were performed with the two histological measures of density of pathologic protein aggregates (Aβ and tau or α-synuclein) as independent variables, while [F-18]FDDNP PET binding value in corresponding region of interest was included as the outcome variable. The value of $p < 0.05$ was considered statistically significant.

Results

Neuropsychological Tests

At the time of imaging experiments the patient revealed a Mini-Mental State Examination score of 20 out of possible 30 points and impairments in several cognitive domains (on tests of recall for simple and complex designs (Benton, 1st percentile and Rey-O, 3rd percentile), as well as visuospatial ability (Rey-O Copy < 1st percentile), language (phonemic fluency, FAS, 1st percentile; semantic fluency, Animals, < 1st percentile) and psychomotor speed

and scanning (Trails A < 1st percentile); both verbal and written perseverations and apparent difficulties initiating motor actions during Rey-O Copy test were described).

Pre mortem Imaging Results

CT scans showed generalized cerebral atrophy with widening of sulci and shrinking of gyri. Ventricles were only moderately enlarged. [F-18]FDG PET scans revealed symmetric generalized cortical hypometabolism, involving parietal, prefrontal, temporal, occipital and posterior cingulate cortices as well as in sensorimotor cortex. Relative preservation of metabolism was seen in subcortical structures (basal ganglia, thalamus) and cerebellum. The pattern of metabolism was consistent with the presence of a primary neurodegenerative dementia but hypometabolism in the occipital cortex strongly suggested dementia with LB (Figure 1) [29–31]. Elevated [F-18]FDDNP signal was observed in basal ganglia (DVR 1.47), thalamus (1.39) and several cortical areas with the highest cortical [F-18]FDDNP binding values in the medial temporal lobe (DVR up to 1.26), followed by temporal (1.12 – 1.23), frontal (1.10 – 1.23) and posterior cingulate cortex (1.14). [F-18]FDDNP signal was lowest in the primary sensorimotor (0.95) and occipital cortex (1.02) (Table 1; Figures 1 and 2).

Autopsy Results

The brain was atrophic upon macroscopic examination and depigmentation of substantia nigra was observed. The diagnosis of DLB [32] was confirmed microscopically. Observed under a fluorescence microscope, unlabeled FDDNP was found to label abundant Aβ plaques and diffuse Aβ aggregates (Figures 3A and 4 A, with dense cores of classic senile plaques displaying most prominent fluorescence), NFTs (Figure 4 D, most notably in temporal lobe), as well as LB (Figure 4 G) in both cortical and subcortical areas. Numerous NFT were the predominant type of pathology seen in the structures of medial temporal lobe, and both, Aβ aggregates and NFT were seen through the temporal neocortex. Aβ aggregates predominated in the rest of the neocortex, and they were least frequent in the sensorimotor and occipital cortex, consistent with imaging results.

Widespread pathology distribution was confirmed using Thioflavin S fluorescence. Numerous LB in brainstem structures, most notably in substantia nigra, were revealed by α-synuclein IHC and IF labeling. Several cortical regions were also affected; their density was highest in the posterior cingulate gyrus (2 – 3 LB per low power magnification field) and few were found in the temporal cortex (Figure 4 H). In general, observed densities of cortical LBs were much lower than those of Aβ and hyperphosphorylated tau accumulation. Sensorimotor and occipital cortices were the least affected regions by both, Aβ and hyperphosphorylated tau accumulation, visualized using IHC. Aβ was found in all examined gray matter regions in the form of classic SP (dense-core plaques) or, most abundantly, as diffuse deposits consistent with earlier pathological observations in LBD patients [17]. Frontal cortex and posterior cingulate gyrus were most prominently affected with density of Aβ IHC deposits reaching up to 2.6 and 1.9 times higher values than those measured in the sensorimotor cortex, respectively (Table 1, Figure 3B). Hyperphosphorylated tau deposit distribution was consistent with Braak stage IV–V [13]. Tau-immunoreactive optical density signal was highest in the structures of the medial temporal lobe, where it reached 14.7 times higher values than that measured in the primary sensorimotor cortex. Inferior and middle temporal gyrus and some areas of the frontal cortex were also heavily affected by hyperphoshorylated tau deposition, the former displaying over ten times and the latter over six times more hyperphosphorylated tau density relative to the primary sensorimotor cortex (Table 1, Figure 3B). Subcortical structures are visible only in one cut (Figure 2, level III) including putamen, globus pallidus, tail of caudate, and several thalamic nuclei and were not included in the correlational analysis. Visual inspection reveals presence of Aβ IHC with

variable densities in low range in all basal ganglia structures and in thalamic nuclei. Hyperphosphorylated tau IHC was apparent in putamen and in tail of caudate but not in other subcortical areas.

Co-localization analysis of FDDNP histofluorescent labeling and Aβ IF detection in SP (n=154) with microscopy showed that both, FDDNP signal and IF fluorescence predominantly overlapped (Figure 4 A–C) with high co-localization coefficients (m1=88.8, m2=82.0). Hyperphosphorylated tau IF signal was more extensive when compared with FDDNP fluorescence in NFT (n=163) labeling, resulting in lower co-localization coefficient, however the FDDNP signal was predominantly localized in IF-positive areas (Figure 4 D–F) (m1=82.1, m2=65.0). Over 90% of FDDNP fluorescent signal in FDDNP-labeled LB (n=32) was localized inside areas of alpha-synuclein IF. Immunolabeling of LB was more extensive and resulted in lower IF to FDDNP co-localization coefficient (Figure 4) (m1=98.0, m2=49.9).

Digital autoradiography using [F-18]FDDNP confirmed high tracer labeling in the temporal cortex, posterior cingulate gyrus and regions of the frontal cortex (Figure 1 F, K). Primary motor and sensory cortices displayed the lowest [F-18]FDDNP signal. The distribution of the signal was in accordance with microscopically observed FDDNP fluorescent labeling of senile plaques and NFT and the distribution of Aβ and hyperphosphorylated tau pathology, visualized immunohistochemically on whole-brain coronal sections.

No correlation was found between [F-18]FDG PET SUVR values and estimated optical density of Aβ or hyperphosphorylated tau immunoreactive signal in the analyzed ROIs (R^2=0.024 and R^2=0.006, respectively). [F-18]FDDNP PET DVRs however, correlated significantly with the IHC determined density of the predominant pathology type. High correlation between Aβ deposit density in the frontal cortex and posterior cingulate gyrus with [F-18]FDDNP PET binding values was observed (p<0.001, slope 0.017, R=0.97, R^2=0.94). Likewise, the correlation between hyperphosphorylated tau immunoreactive signal density and [F-18]FDDNP PET DVRs in the temporal lobe was also highly significant (p<0.001, slope 0.0033, R=0.87, R^2=0.76). Not surprisingly, there was no co-linearity between Aβ density and hyperphosphorylated tau deposits density. Multiple regression analysis revealed that a combination of predicted [F-18]FDDNP DVR values calculated from Aβ and from hyperphosphorylated tau immunoreactive signal densities was highly predictive of measured [F-18]FDDNP PET DVR throughout analyzed ROI (predicted vs. measured [F-18]FDDNP DVR: p<0.0001, slope 0.476, R=0.92, R^2=0.85). Both, Aβ and hyperphosphorylated tau deposits contributed significantly to the regression model (both p < 0.001) and this model described [F-18]FDDNP PET signal distribution through all analyzed ROI better than either NFT or Aβ plaque distribution alone.

Discussion

Formation of insoluble fibrils via β-pleated sheet polymerization of different proteins and their deposition in different brain regions are pathological changes observed in many neurodegenerative diseases, e.g., Aβ plaques and NFT in AD and DLB. Brain pathology of DLB consists of LB in cortex and subcortical regions and, in most cases, by presence of varying degrees of Alzheimer-type pathology, i.e. Aβ plaques and NFTs [33, 34]; however NFT densities are often significantly lower than those observed in AD [35]. Patients with copious NFT formation typically present with a clinical picture of AD with fewer DLB clinical characteristics than those with few or no hyperphosphorylated tau deposits [36]. Also, classical brain glucose hypometabolism patterns as measured by [F-18]FDG PET usually confirms DLB and AD [29–30]. DLB and AD metabolism patterns overlap in the neocortex with the exception of visual cortex which is typically hypometabolic in DLB but

not in AD. In this studied case, abundant NFT and rich Aβ pathology closely mimic general AD-related distribution of pathology. However, presence of Lewy bodies in the brainstem, limbic areas and neocortex as well as decreased [F-18]FDG SUVR values in the occipital, parietal and temporal lobes and in posterior cingulate gyrus, , present findings typical of DLB (Tables 1 and 2). These combined results indicate DLB and AD co-morbidity.

Regional brain correlation of *in vivo* deposition of PET imaging probes targeting tau, Aβ deposition and other proteinaceous lesions with the distribution of targeted pathology and its densities obtained *post mortem* is an important step in validation of these imaging techniques for use in living subjects. Previous methods, however, have relied upon microscopic immunohistochemistry determinations in limited number of brain areas for comparison with imaging data, but this approach has the limitation of bias samplings. To date one biopsy study [37] and several autopsy studies have reported correlation of pathology with N-methyl [^{11}C]2-(4'-methylaminophenyl)-6-hydroxybenzothiazole ([C-11]PIB) imaging results in subjects with AD [38–42] and DLB [17], among others. Similar comparison of imaging results using the stilbene-based florbetapir in a DLB patient was recently reported by Sabbagh *et al* [43]. With the exception of the study by Ikonomovic *et al* [38], using only one brain slice, none of these studies has mapped out Aβ pathologies in sufficient hemispheric detail to allow for regional cortical correlation of the imaging signal with underlying pathology throughout the brain, irrespective of the neurodegenerative disease.

This work reports such a correlation using a 3-D brain hemisphere approach in the first autopsy-confirmed DLB patient who underwent *pre mortem* [F-18]FDDNP PET. [F-18]FDDNP PET scan results, together with CT and [F-18]FDG PET results, were consistent with a primary neurodegenerative dementia and provided the basis for the patient's diagnosis. DLB with prominent Aβ and hyperphosphorylated tau pathology was confirmed *post mortem* during autopsy 46 months after the patient received his PET scans. [F-18]FDDNP DVRs were increased in all areas of the neocortex and the reported values are well within the range reported for AD subjects [5]. When compared with IHC results, it becomes obvious that both types of pathology are present in different cortical brain regions albeit in different proportions. For example, high [F-18]FDDNP PET DVR was observed both in Aβ rich frontal cortex and cingulate gyrus and in hyperphosphorylated tau aggregate rich medial temporal lobe structures (Figure 5). It is not surprising that linear combination of both Aβ and tau immunoreactive signal densities, as calculated by the multiple linear regression analysis, strongly correlated with the [F-18]FDDNP PET binding pattern in this investigation. Additive contribution of both types of pathology is most evident in the neocortical areas of temporal cortex with mixed pathology profile (Figure 2, levels III and IV) and the role of both major types of pathology in [F-18]FDDNP PET was supported by fluorescence microscopy and autoradiography (Figures 3 and 4). As this paper was designed as a 3-D brain method of neuropathology evaluation using imaging in comparison with *postmortem* autopsy in cortical areas following the established ABC criteria for neuropathological diagnosis of Alzheimer's (references 9–11), no quantitative correlative analysis with IHC data of subcortical areas was performed. As such, the brain tissue was sampled at five levels (Figure 2) to cover different cortical areas but with only limited sampling of subcortical structures. The observed [F-18]FDDNP DVR values in striatum and thalamus in this patient were similar to those recently reported for PSP (striatum: 1.443±0.102; thalamus: 1.478±0.070) and significantly higher than those observed in controls or patients with Parkinson's disease (DVR values in both groups < 1.250 in striatum and thalamus) [59].

[F-18]FDDNP digital autoradiography findings of high tracer activity in the cingulate gyrus, as well as temporal and frontal cortex are in accordance with previously reported results [2].

They are also congruent with *in vivo* [F-18]FDDNP PET binding values distribution in the cerebral cortex of this patient. At the microscopic level, co-localization analysis (Figure 4) confirmed fluorescent FDDNP labeling of all three types of protein aggregates in the analyzed brain tissue – abundant SP, as well as NFT and LB. NFT associated with AD are known to label with FDDNP *in vitro* [2] and showed the most reliable fluorescent FDDNP labeling of all hyperphosphorylated tau deposits in a recent histochemical study of conformational neurodegenerative disorders [3]. That same work also reported that 58% of cortical LB was labeled with FDDNP *in vitro*. Convincing FDDNP histofluorescence co-localization with α-synuclein IF signal was determined in the present study and these α-synuclein aggregates may potentially contribute to the *in vivo* [F-18]FDDNP signal. However, LB aggregates are small in size and they are scarce in comparison with NFT or senile plaques in this patient (Figure 4 G). At autopsy the α-synuclein histochemically labeled area represented less than 1% of the Aβ area in the present case, which is in accordance with previous estimates of Aβ SP occupying 30-fold greater areas in histological brain sections of DLB that those of α-synuclein deposits [44]. LB contribution to the [F-18]FDDNP-PET signal in the present case may thus be small or even negligible. Additionally, LB occurred most frequently in the posterior cingulate gyrus and lateral temporal cortex, areas with abundant Aβ deposition. This overlap in distribution rendered the potential contribution of α-synuclein to *in vivo* [F-18]FDDNP PET cortical binding values low.

There was no direct regional correlation between cortical hypometabolism (detected using [F-18]FDG PET) and either Aβ SP or NFT distribution. This is to be expected, however. Although imaging of fibrillar deposits has its role in the diagnosis of neurodegenerative diseases based on the pattern of distribution of these lesions it is still not fully understood how pathology distribution and densities contribute to cellular neurodegeneration which leads to disease symptomatology. Functional measures depend on the activity of brain networks which are affected by neurodegenerative changes at the level of synapses and neurons forming these circuits, whereas density of Aβ SP and hyperphosphorylated tau immunoreactive signals, depend on the presence of specific epitopes in relevant brain regions, which may not coincide with all parts of these functional networks [45–47]. Thus it is not surprising that posterior cingulate gyrus hypometabolism can be observed in very early AD [48] when pathological changes are still limited to the projecting medial temporal lobe. The characteristic occipital hypometabolism, also described in this patient, is not associated with aberrant protein deposits in the hypometabolic brain regions, but rather with widespread spongiform change and gliosis in long projection fibers [49], that could be the consequence of pathological processes in the brainstem or basal forebrain structures [50]. In this patient, occipital hypometabolism was associated with low [F-18]FDDNP DVRs and absence of aberrant protein aggregates in this brain region was evident during tissue analysis at autopsy. Therefore, we have to interpret regional comparisons of functional and structural measurement results with extreme caution.

It is also worth noting that the subject had significant level of cortical atrophy visible as dilation of major ventricles, widening of sulci and shrinking of gyri on CT scan. This atrophy is indicative of advanced stage of pathological changes in the brain which was also obvious from the extensive cortical hypometabolism pattern. We also have to take into account the effect that severe atrophy and partial volume effects would have on [F-18]FDG and [F-18]FDDNP PET signals. Due to the relatively low resolution of PET cameras (~4 mm), both gray matter loss and widening of gyri would contribute to dilution of the PET signal. Correction of these partial volume effects does make the true [F-18]FDDNP DVR more robust and pathology correlations even more reliable. Conversely, hypometabolic measures via [F-18]FDG SUVRs would be tempered significantly when partial volume effects corrections for atrophy are performed [51].

Visual comparison of atrophy levels observed on CT and the shape of brain tissue sections after 46 months at the autopsy shows good matching of shapes and limited atrophy between these two points. This is consistent with the slow progression of dementia-associated pathology burden in patients with late AD by comparing densities of SP and NFT at biopsy and autopsy [52–54]. Statistically significant progression of SP and NFT burden was described only in two out of four patients in a study with the longest time period form biopsy to autopsy (9–11 years) [54], while other studies of five [52] and four [53] patients, with a follow up of 3 to 7 years and 21 to 47 months, respectively, showed only non-significant changes in densities of cortical SP and NFT in the frontal and temporal cortex where the biopsy samples were collected. On the other hand, as expected, evidence of continuous pathology accumulation can be seen early in the course of the disease [5].

In conclusion, the results of the present study offer validation of [F-18]FDDNP PET as an imaging agent for neuropathology distribution (Aβ and tau deposits), as confirmed *post mortem* with IHC determinations in three physical dimensions in whole brain coronal sections (Figure 2), and further confirmed with microscopy and autoradiographic determinations (Figure 3). Due to the low overall load of α-synuclein deposits, the *in vivo* contribution of their labeling remained quantitatively insignificant in the analyzed case, despite reliable FDDNP labeling of LB *in vitro*. Due to its ability to label both Aβ deposits and NFT, [F-18]FDDNP offers high sensitivity for early detection of AD related pathology when changes appear predominantly in the form of NFT even before dementia symptoms are observable [55, 56]. [F-18]FDDNP sensitivity for brain tau aggregates has permitted histochemical correlates previously unrealized with tau pathology. Moreover, this [F-18]FDDNP sensitivity allows identification of early affected subjects and increases the window of opportunity for therapeutic intervention at the early stages of dementia when cellular damage is still contained. [F-18]FDDNP PET could also be used for monitoring of dementia-associated pathology loads in patients involved in anti-aggregation therapeutic intervention trials, most intriguingly anti-tau therapies [57].This use of [F-18]FDDNP PET is further supported by recent co-crystallization of DDNP with tau fragments in X-ray microcrystallography at atomic resolution [58].

Acknowledgments

References

1. Shoghi-Jadid K, Small GW, Agdeppa ED, Kepe V, Ercoli LM, Siddarth P, Read S, Satyamurthy N, Petric A, Huang S-C, Barrio JR. Localization of neurofibrillary tangles and beta-amyloid plaques in the brains of living patients with Alzheimer disease. Am J Geriatr Psychiatry. 2002; 10:24–35. [PubMed: 11790632]

2. Agdeppa ED, Kepe V, Liu J, Flores-Torres S, Satyamurthy N, Petric A, Cole GM, Small GW, Huang S-C, Barrio JR. Binding characteristics of radiofluorinated 6-dialkylamino-2-naphthylethylidene derivatives as positron emission tomography imaging probes for beta-amyloid plaques in Alzheimer's disease. J Neurosci. 2001; 21:RC189. [PubMed: 11734604]

3. Smid LM, Vovko TD, Popovic M, Petric A, Kepe V, Barrio JR, Vidmar G, Bresjanac M. The 2,6-disubstituted naphthalene derivative FDDNP labeling reliably predicts Congo red birefringence of protein deposits in brain sections of selected human neurodegenerative diseases. Brain Pathol. 2006; 16:124–130. [PubMed: 16768752]

4. Bresjanac M, Smid LM, Vovko TD, Petric A, Barrio JR, Popovic M. Molecular-imaging probe 2-(1-[6-[(2-fluoroethyl)(methyl)amino]-2-naphthyl]ethylidene) malononitrile labels prion plaques in vitro. J Neurosci. 2003; 23:8029–8033. [PubMed: 12954864]

5. Small GW, Kepe V, Ercoli LM, Siddarth P, Bookheimer SY, Miller KJ, Bookheimer SY, Lavretsky H, Cole G, Vinters HV, Thompson P, Huang S-C, Satyamurthy N, Phelps ME, Barrio JR. PET of brain amyloid and tau in mild cognitive impairment. N Engl J Med. 2006; 355:2652–2663. [PubMed: 17182990]

6. Kepe V, Ghetti B, Farlow MR, Bresjanac M, Miller K, Huang S-C, Wong K-P, Murrell JR, Piccardo P, Epperson F, Repovš G, Smid LM, Petric A, Siddarth P, Liu J, Satyamurthy N, Small GW, Barrio JR. PET of Brain Prion Protein Amyloid in Gerstmann-Sträussler-Scheinker Disease. Brain Pathol. 2010; 20:419–430. [PubMed: 19725833]

7. Ghetti B, Kepe V, Murrell JR, Farlow MR, Epperson F, Bresjanac M, Repovs G, Smid LM, Popovic M, Petric A, Sung H, Small GW, Satyamurthy N, Phelps ME, Barrio JR. Visualization of prion pathology in the living brain of Gerstmann-Straussler-Scheinker disease patients using [F-18] FDDNP PET. Brain Pathol. 2006; 16(Suppl S1):S9–S017.

8. Boxer AL, Rabinovici GD, Kepe V, Goldman J, Furst AJ, Huang S-C, Baker SL, Chui H, Geschwind MD, Small GW, Barrio JR, Jagust W, Miller BL. Amyloid imaging in distinguishing atypical prion disease from Alzheimer disease. Neurology. 2007; 69:283–290. [PubMed: 17636066]

9. Montine TJ, Phelps CH, Beach TG, Bigio EH, Cairns NJ, Dickson DW, Duyckaerts C, Frosch MP, Masliah E, Mirra SS, Nelson PT, Schneider JA, Thal DR, Trojanowski JQ, Vinters HV, Hyman BT. National Institute on Aging-Alzheimer's Association guidelines for the neuropathologic assessment of Alzheimer's disease: a practical approach. Acta Neuropathol. 2012; 123:1–11. [PubMed: 22101365]

10. Hyman BT, Phelps CH, Beach TG, Bigio EH, Cairns NJ, Carrillo MC, Dickson DW, Duyckaerts C, Frosch MP, Masliah E, Mirra SS, Nelson PT, Schneider JA, Thal DR, Thies B, Trojanowski JQ, Vinters HV, Montine TJ. Institute on Aging-Alzheimer's Association guidelines for the neuropathologic assessment of Alzheimer's disease. Alzheimers Dement. 2012; 8:1–13. [PubMed: 22265587]

11. Thal DR, Rüb U, Orantes M, Braak H. Phases of A beta-deposition in the human brain and its relevance for the development of AD. Neurology. 2002; 58:1791–1800. [PubMed: 12084879]

12. Protas HD, Huang SC, Kepe V, Hayashi K, Klunder A, Braskie MN, Ercoli L, Bookheimer SY, Thompson PM, Small GW, Barrio JR. FDDNP binding using MR derived cortical surface maps. Neuroimage. 2010; 49:240–248. [PubMed: 19703569]

13. Braak H, Alafuzoff I, Arzberger T, Kretzschmar H, Del Tredici K. Staging of Alzheimer disease-associated neurofibrillary pathology using paraffin sections and immunocytochemistry. Acta Neuropathol. 2006; 112:389–404. [PubMed: 16906426]

14. Teng E, Kepe V, Frautschy SA, Liu J, Satyamurthy N, Yang F, Chen P-P, Jones MR, Huang S-C, Flood DG, Trusko SP, Small GW, Cole GM, Barrio JR. [F-18]FDDNP microPET imaging correlates with brain Aβ burden in a transgenic rat model of Alzheimer disease: Effects of aging, *in vivo* blockade, and anti-Aβ antibody treatment. Neurobiol Dis. 2011; 43:565–575. [PubMed: 21605674]

15. Flood DG, Lin YG, Lang DM, Trusko SP, Hirsch JD, Savage MJ, Scott RW, Howland DS. A transgenic rat model of Alzheimer's disease with extracellular Abeta deposition. Neurobiol Aging. 2009; 30:1078–1090. [PubMed: 18053619]

16. Liu L, Orozco IJ, Planel E, Wen Y, Bretteville A, Krishnamurthy P, Wang L, Herman M, Figueroa H, Yu WH, Arancio O, Duff K. A transgenic rat that develops Alzheimer's disease-like amyloid pathology, deficits in synaptic plasticity and cognitive impairment. Neurobiol Dis. 2008; 31:46–57. [PubMed: 18504134]

17. Kantarci K, Yang C, Schneider JA, Senjem ML, Reyes DA, Lowe VJ, Barnes LL, Aggarwal NT, Bennett DA, Smith GE, Petersen RC, Jack CR Jr, Boeve BF. Ante mortem amyloid imaging and β-amyloid pathology in a case with dementia with Lewy bodies. Neurobiol Aging. 2010; 33:878–885. [PubMed: 20961664]

18. Folstein MF, Folstein SE, McHugh PR. "Mini-mental state". A practical method for grading the cognitive state of patients for the clinician. J Psychiatr Res. 1975; 12:189–198. [PubMed: 1202204]

19. Lezak, MD.; Howieson, DB.; Loring, DW.; Hannay, HJ.; Fischer, JS. Neuropsychological Assessment. 4th ed.. OUP USA: 2004.

20. Liu J, Kepe V, Zabjek A, Petric A, Padgett HC, Satyamurthy N, Barrio JR. High-yield, automated radiosynthesis of 2-(1-6-[(2-[18F]fluoroethyl)(methyl)amino]-2-naphthylethylidene)malononitrile ([18F]FDDNP) ready for animal or human administration. Mol Imaging Biol. 2007; 9:6–16. [PubMed: 17051324]

21. Andersson JL, Vagnhammar BE, Schneider H. Accurate attenuation correction despite movement during PET imaging. J Nucl Med. 1995; 36:670–678. [PubMed: 7699463]

22. Wardak M, Wong KP, Shao W, Dahlbom M, Kepe V, Satyamurthy N, Small GW, Barrio JR, Huang SC. Movement correction method for human brain PET images: application to quantitative analysis of dynamic 18F-FDDNP scans. J Nucl Med. 2010; 51:210–218. [PubMed: 20080894]

23. Kepe V, Barrio JR, Huang S, Ercoli L, Siddarth P, Shoghi-Jadid K, Cole GM, Satyamurthy N, Cummings JL, Small GW, Phelps ME. Serotonin 1A receptors in the living brain of Alzheimer's disease patients. Proc Natl Acad Sci USA. 2006; 103:702–707. [PubMed: 16407119]

24. Logan J, Fowler JS, Volkow ND, Wang GJ, Ding YS, Alexoff DL. Distribution volume ratios without blood sampling from graphical analysis of PET data. J Cereb Blood Flow Metab. 1996; 16:834–840. [PubMed: 8784228]

25. Loening AM, Gambhir SS. AMIDE: a free software tool for multimodality medical image analysis. Mol Imaging. 2003; 2:131–137. [PubMed: 14649056]

26. Agdeppa ED, Kepe V, Petri A, Satyamurthy N, Liu J, Huang SC, Small GW, Cole GM, Barrio JR. In vitro detection of (S)-naproxen and ibuprofen binding to plaques in the Alzheimer's brain using the positron emission tomography molecular imaging probe 2-(1-[6-[(2-[(18)F]fluoroethyl) (methyl)amino]-2-naphthyl]ethylidene)malononitrile. Neuroscience. 2003; 117:723–730. [PubMed: 12617976]

27. Sun A, Nguyen XV, Bing G. Comparative analysis of an improved thioflavin-s stain, Gallyas silver stain, and immunohistochemistry for neurofibrillary tangle demonstration on the same sections. J Histochem Cytochem. 2002; 50:463–472. [PubMed: 11897799]

28. Manders EMM, Verbeek FI, Aten IA. Measurement of co-localization of objects in dual-colour confocal images. J Microscopy. 1993; 169:375–382.

29. Minoshima S, Foster NL, Sima AA, Frey KA, Albin RL, Kuhl DE. Alzheimer's disease versus dementia with Lewy bodies: cerebral metabolic distinction with autopsy confirmation. Ann Neurol. 2001; 50:358–365. [PubMed: 11558792]

30. Gilman S, Koeppe RA, Little R, An H, Junck L, Giordani B, Persad C, Heumann M, Wernette K. Differentiation of Alzheimer's disease from dementia with Lewy bodies utilizing positron emission tomography with [18F]fluorodeoxyglucose and neuropsychological testing. Exp Neurol. 2005; 191(Suppl 1):S95–S103. [PubMed: 15629765]

31. Ishii K, Imamura T, Sasaki M, Yamaji S, Sakamoto S, Kitagaki H, Hashimoto M, Hirono N, Shimomura T, Mori E. Regional cerebral glucose metabolism in dementia with Lewy bodies and Alzheimer's disease. Neurology. 1998; 51:125–130. [PubMed: 9674790]

32. McKeith IG, Galasko D, Kosaka K, Perry EK, Dickson DW, Hansen LA, Salmon DP, Lowe J, Mirra SS, Byrne EJ, Lennox G, Quinn NP, Edwardson JA, Ince PG, Bergeron C, Burns A, Miller BL, Lovestone S, Collerton D, Jansen EN, Ballard C, deVos RA, Wilcock GK, Jellinger KA, Perry RH. Consensus guidelines for the clinical and pathologic diagnosis of dementia with Lewy bodies (DLB): report of the consortium on DLB international workshop. Neurology. 1996; 47:1113–1124. [PubMed: 8909416]

33. Dickson DW. Dementia with Lewy bodies: neuropathology. J Geriatr Psychiatry Neurol. 2000; 15:210–216. [PubMed: 12489917]

34. Ballard C, Ziabreva I, Perry R, Larsen JP, O'Brien J, McKeith I, Perry E, Aarsland D. Differences in neuropathologic characteristics across the Lewy body dementia spectrum. Neurology. 2006; 67:1931–1934. [PubMed: 17159096]

35. McKeith I, Mintzer J, Aarsland D, Burn D, Chiu H, Cohen-Mansfield J, Dickson D, Dubois B, Duda JE, Feldman H, Gauthier S, Halliday G, Lawlor B, Lippa C, Lopez OL, Carlos Machado J, O'Brien J, Playfer J, Reid W. International Psychogeriatric Association Expert Meeting on DLB. Dementia with Lewy bodies. Lancet Neurol. 2004; 3:19–28. [PubMed: 14693108]

36. Merdes A, Hansen L, Jeste D, Galasko D, Hofstetter C, Ho G, Thal LJ, Corey-Bloom J. Influence of Alzheimer pathology on clinical diagnostic accuracy in dementia with Lewy bodies. Neurology. 2003; 60:1586–1590. [PubMed: 12771246]

37. Leinonen V, Alafuzoff I, Aalto S, Suotunen T, Savolainen S, Någren K, Tapiola T, Pirttilä T, Rinne J, Jääskeläinen JE, Soininen H, Rinne JO. Assessment of beta-amyloid in a frontal cortical brain biopsy specimen and by positron emission tomography with carbon 11-labeled Pittsburgh Compound B. Arch Neurol. 2008; 65:1304–1309. [PubMed: 18695050]

38. Ikonomovic MD, Klunk WE, Abrahamson EE, Mathis CA, Price JC, Tsopelas ND, Lopresti BJ, Ziolko S, Bi W, Paljug WR, Debnath ML, Hope CE, Isanski BA, Hamilton RL, DeKosky ST. Post-mortem correlates of in vivo PiB-PET amyloid imaging in a typical case of Alzheimer's disease. Brain. 2008; 131:1630–1645. [PubMed: 18339640]

39. Kadir A, Marutle A, Gonzalez D, Schöll M, Almkvist O, Mousavi M, Mustafiz T, Darreh-Shori T, Nennesmo I, Nordberg A. Positron emission tomography imaging and clinical progression in relation to molecular pathology in the first Pittsburgh Compound B positron emission tomography patient with Alzheimer's disease. Brain. 2011; 134:301–317. [PubMed: 21149866]

40. Bacskai BJ, Frosch MP, Freeman SH, Raymond SB, Augustinack JC, Johnson KA, Irizarry MC, Klunk WE, Mathis CA, DeKosky ST, Hyman BT, Growdon JH. Molecular imaging with Pittsburgh Compound B confirmed at autopsy: a case report. Arch Neurol. 2007; 64:431–434. [PubMed: 17353389]

41. Cairns NJ, Ikonomovic MD, Benzinger T, Storandt M, Fagan AM, Shah AR, Reinwald LT, Carter D, Felton A, Holtzman DM, Mintun MA, Klunk WE, Morris JC. Absence of Pittsburgh compound B detection of cerebral amyloid beta in a patient with clinical, cognitive, and cerebrospinal fluid markers of Alzheimer disease: a case report. Arch Neurol. 2009; 66:1557–1562. [PubMed: 20008664]

42. Ikonomovic MD, Abrahamson EE, Price JC, Hamilton RL, Mathis CA, Paljug WR, Debnath ML, Cohen AD, Mizukami K, Dekosky ST, Lopez OL, Klunk WE. Early AD pathology in a [C-11]PiB-negative case: a PiB-amyloid imaging, biochemical, and immunohistochemical study. Acta Neuropathol. 2012; 123:433–447. [PubMed: 22271153]

43. Sabbagh MN, Fleisher A, Chen K, Rogers J, Berk C, Reiman E, Pontecorvo M, Mintun M, Skovronsky D, Jacobson SA, Sue LI, Liebsack C, Charney AS, Cole L, Belden C, Beach TG. Positron emission tomography and neuropathologic estimates of fibrillar amyloid-β in a patient with Down syndrome and Alzheimer disease. Arch Neurol. 2011; 68:1461–1466. [PubMed: 22084131]

44. Fodero-Tavoletti MT, Smith DP, McLean CA, Adlard PA, Barnham KJ, Foster LE, Leone L, Perez K, Cortés M, Culvenor JG, Li QX, Laughton KM, Rowe CC, Masters CL, Cappai R, Villemagne VL. In vitro characterization of Pittsburgh Compound-B binding to Lewy bodies. J Neurosci. 2007; 27:10365–10371. [PubMed: 17898208]

45. Shin J, Kepe V, Small GW, Phelps ME, Barrio JR. Multimodal imaging of Alzheimer pathophysiology in the brain's default mode network. Intl J Alzheimer's Dis. 2011; 2011:687945.

46. Gusnard DA, Raichle ME. Searching for a baseline: functional imaging and the resting human brain. Nat Rev Neurosci. 2001; 2:685–694. [PubMed: 11584306]

47. Andrews-Hanna JR, Reidler JS, Sepulcre J, Poulin R, Buckner RL. Functional-anatomic fractionation of the brain's default network. Neuron. 2010; 65:550–562. [PubMed: 20188659]

48. Minoshima S, Giordani B, Berent S, Frey KA, Foster NL, Kuhl DE. Metabolic reduction in the posterior cingulate cortex in very early Alzheimer's disease. Ann Neurol. 1997; 42:85–94. [PubMed: 9225689]

49. Higuchi M, Tashiro M, Arai H, Okamura N, Hara S, Higuchi S, Itoh M, Shin RW, Trojanowski JQ, Sasaki H. Glucose hypometabolism and neuropathological correlates in brains of dementia with Lewy bodies. Exp Neurol. 2000; 162:247–256. [PubMed: 10739631]

50. Imamura T, Ishii K, Hirono N, Hashimoto M, Tanimukai S, Kazui H, Hanihara T, Sasaki M, Mori E. Occipital glucose metabolism in dementia with lewy bodies with and without Parkinsonism: a study using positron emission tomography. Dement Geriatr Cogn Disord. 2001; 12:194–197. [PubMed: 11244212]

51. Meltzer CC, Leal JP, Mayberg HS, Wagner HN Jr, Frost JJ. Correction of PET data for partial volume effects in human cerebral cortex by MR imaging. J Comput Assist Tomogr. 1990; 14:561–570. [PubMed: 2370355]

52. Mann DM, Marcyniuk B, Yates PO, Neary D, Snowden JS. The progression of the pathological changes of Alzheimer's disease in frontal and temporal neocortex examined both at biopsy and at autopsy. Neuropathol Appl Neurobiol. 1988; 14:177–195. [PubMed: 3405392]

53. Bennett DA, Cochran EJ, Saper CB, Leverenz JB, Gilley DW, Wilson RS. Pathological changes in frontal cortex from biopsy to autopsy in Alzheimer's disease. Neurobiol Aging. 1993; 14:589–596. [PubMed: 8295661]

54. Di Patre PL, Read SL, Cummings JL, Tomiyasu U, Vartavarian LM, Secor DL, Vinters HV. Progression of clinical deterioration and pathological changes in patients with Alzheimer disease evaluated at biopsy and autopsy. Arch Neurol. 1999; 56:1254–1261. [PubMed: 10520942]

55. Price JL, Morris JC. Tangles and plaques in nondemented aging and "preclinical" Alzheimer's disease. Ann Neurol. 1999; 45:358–368. [PubMed: 10072051]

56. Small GW, Siddarth P, Kepe V, Ercoli LM, Burggren AC, Bookheimer SY, Miller KJ, Lavretsky H, Burggren AC, Cole GM, Vinters HV, Thompson PM, Huang SC, Satyamurthy N, Phelps ME, Barrio JR. PET of brain amyloid and tau predicts and tracks cognitive decline in people without dementia. Arch Neurol. 2012; 69:215–222. [PubMed: 22332188]

57. Barrio, JR.; Bordelon, Y.; Small, GW.; Kepe, V. Visualizing tau pathology in the living brain of progressive supranuclear palsy patients. The 10th International Conference on Alzheimer's and Parkinson's Diseases; Barcelona, Spain. 2011.

58. Landau M, Sawaya MR, Faull KF, Laganowsky A, Jiang L, Sievers SA, Liu J, Barrio JR, Eisenberg D. Towards the Amyloid Pharmacophore. PLoS Biology. 2011; 9:e1001080. [PubMed: 21695112]

59. Kepe V, Bordelon Y, Boxer A, Huang SC, Liu J, Thiede FC, Mazziotta JC, Mendez MF, Donoghue D, Small GW, Barrio JR. PET imaging of neuropathology in tauopathies: progressive supranuclear palsy. J Alzheimers Dis. 2013 [Epub ahead of print].
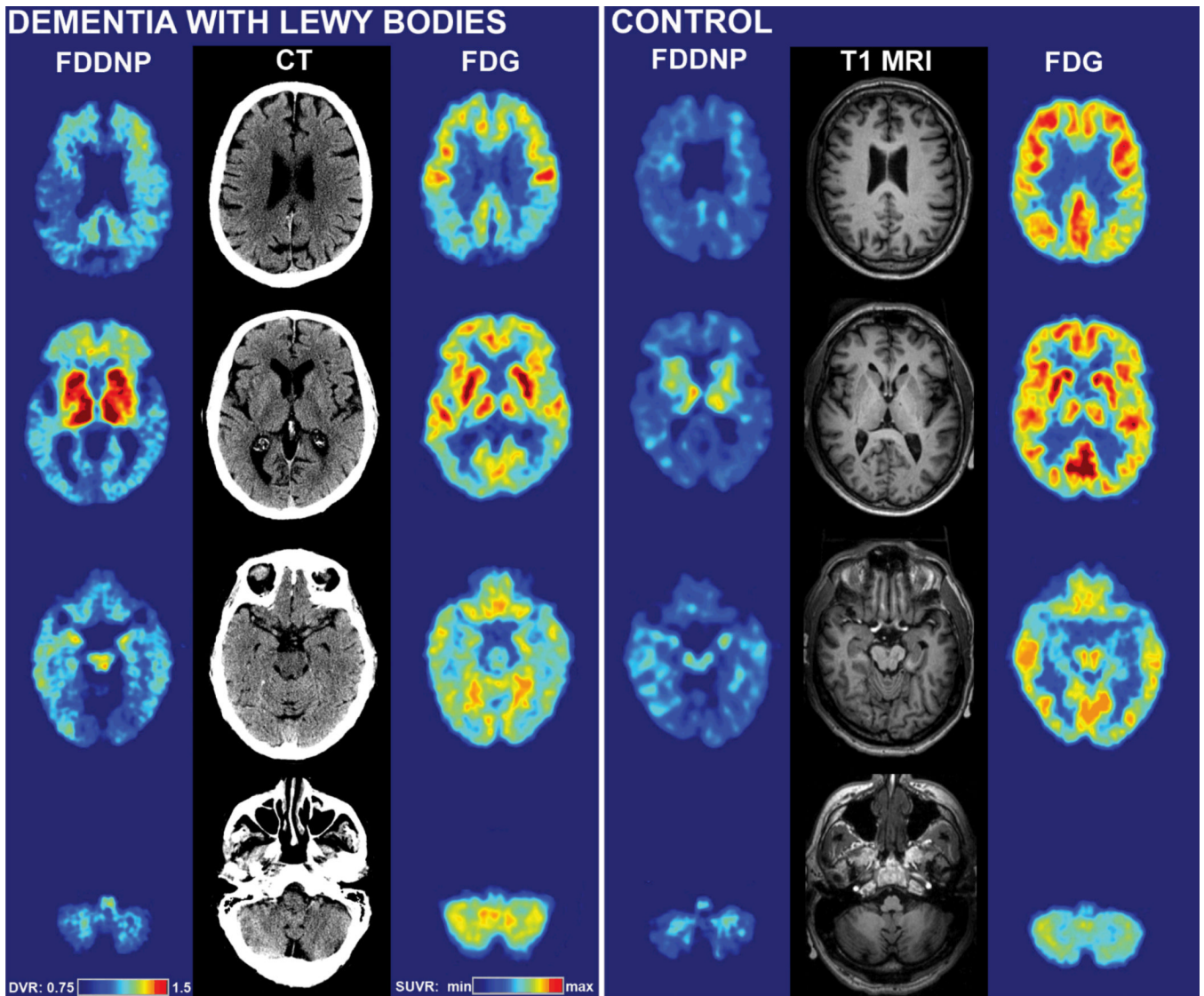
Figure 1.
[F-18]FDDNP-PET and [F-18]FDG-PET images of the DLB subject studied in this paper (left) compared with [F-18]FDDNP-PET and [F-18]FDG-PET images of a 64 year old male control subject without signs of dementia. CT images for the DLB subject and T1 MRI images for the control subject are provided for anatomical reference. Highest [F-18]FDDNP-PET signal in the DLB subject is seen in parts of the frontal cortex and medial temporal lobe. Primary somatosensory cortex is associated with lower [F-18]FDDNP binding. [F-18]FDG-PET revealed global cortical hypometabolism, which includes the occipital region, indicative of DLB. The slices shown in this Figure were obtained at approximately −30° angle to canto-meatal line.
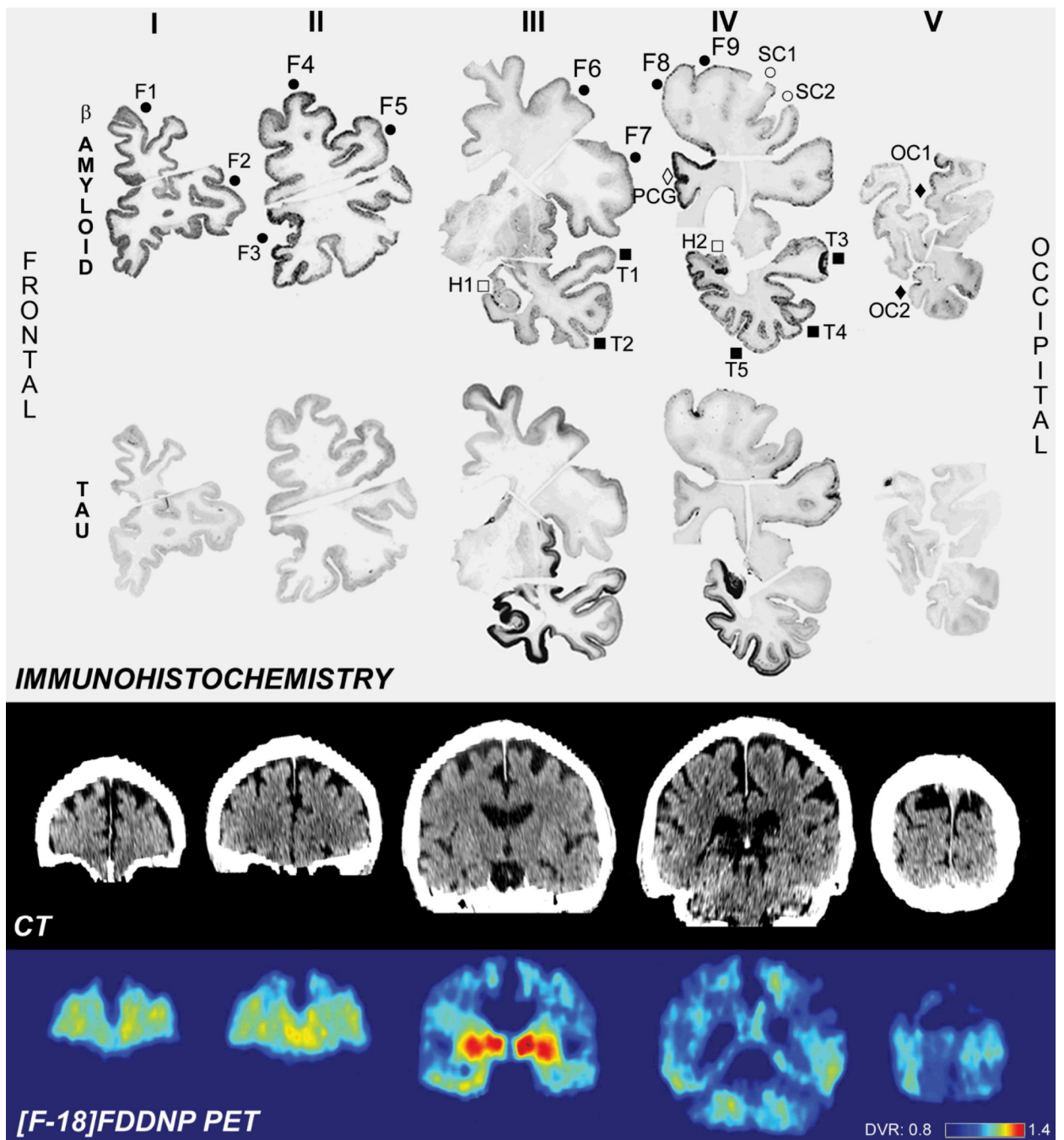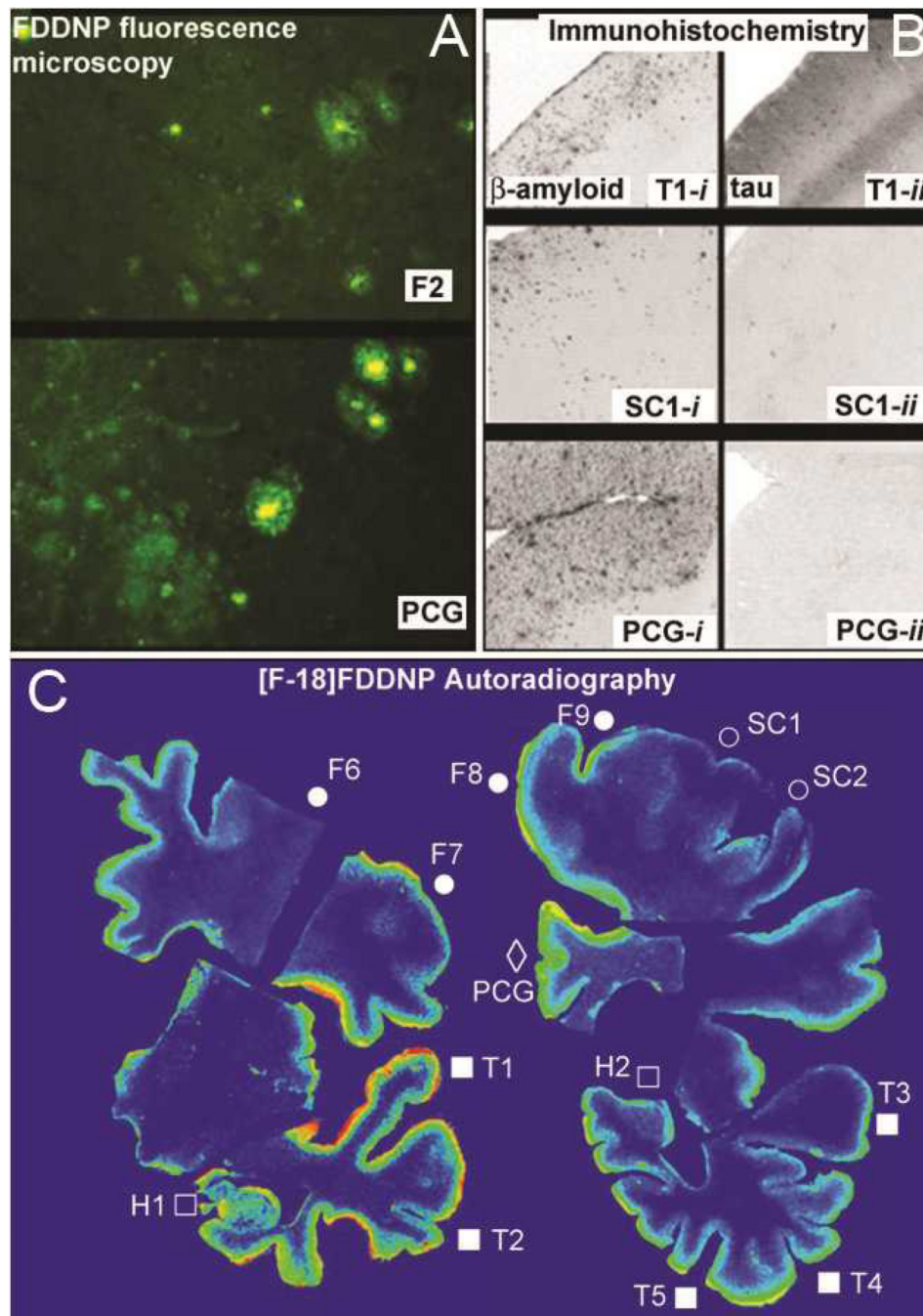
Figure 2.
Comparison of Aβ and hyperphoshorylated tau immunohistochemical labeling and
[F-18]FDDNP PET signal in coronal slices. The results of IHC are shown in the upper two
rows and 21 regions of interest used for quantitative analysis are indicated on Aβ- IHC brain
slices (top row, labels identical to those used in the Table).
Dense deposits of Aβ were detected in frontal lobe, posterior cingulate gyrus and temporal
lobe. Occipital lobe and somatosensory cortex showed lowest level of Aβ IHC labeling.
Hyperphosphorylated tau IHC labeled densely hippocampus and related areas in medial
temporal lobe as well as other neocortical areas of temporal lobe. Frontal cortex showed less

accumulation of hyperphosphorylated tau. Occipital lobe, somatosensory cortex and posterior cingulate gyrus showed only very low level of hyperphosphorylated tau IHC. [F-18]FDDNP signal is the strongest in frontal (Aβ) and temporal (Aβ and tau) lobes as well as posterior cingulate gyrus (Aβ) pointing to contribution of both pathologies to the *in vivo* [F-18]FDDNP signal.

Symbols: full circles = F; open circles = SC; full squares = T; open squares = H; full diamond = OC; open diamond = PCG.
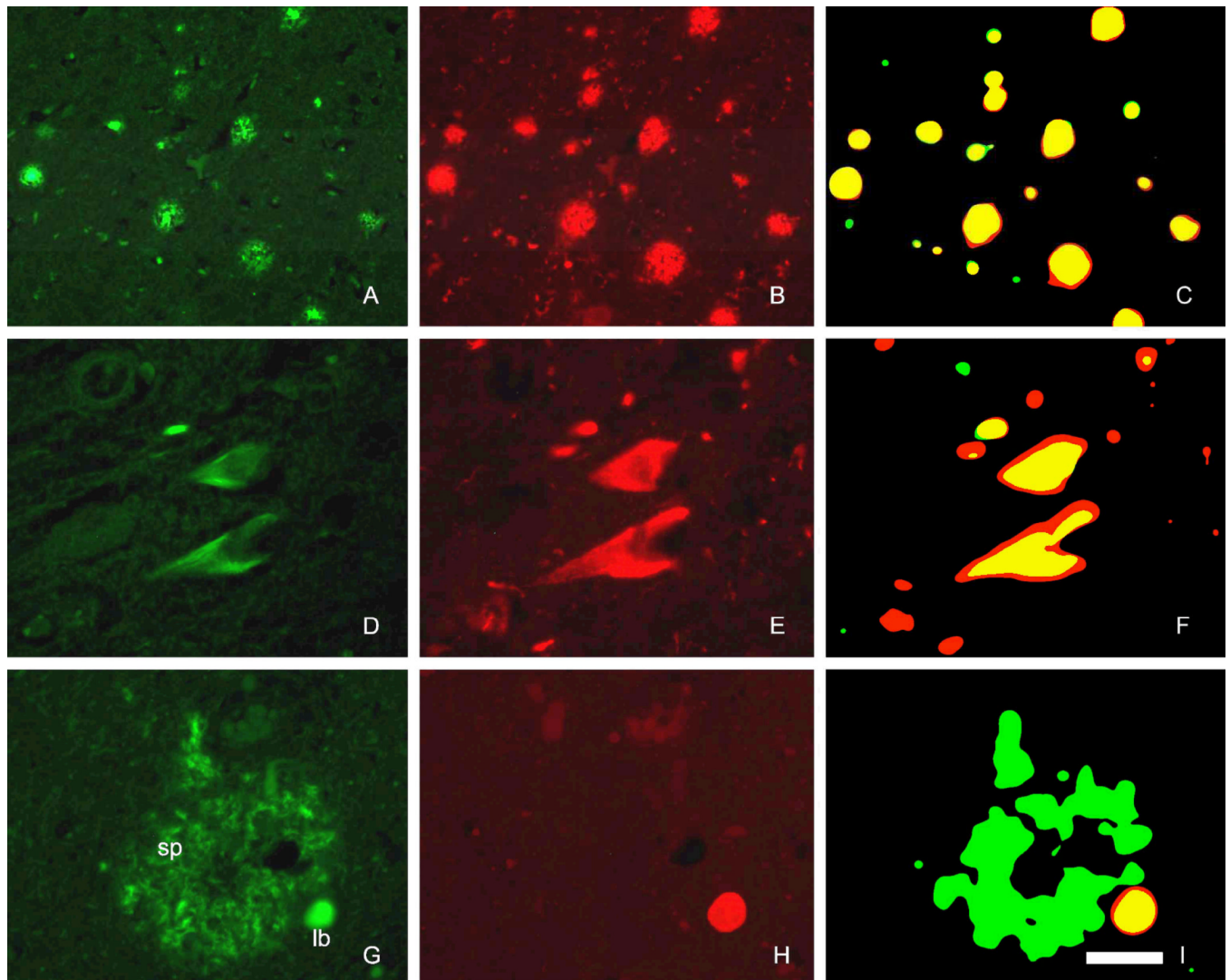
Figure 3.
In vitro dementia-related pathology detection, using FDDNP labeling and immunohistochemistry (IHC). A: FDDNP fluorescence microscopy of abundant Aβ deposits in frontal cortex (F2) and cingulateg gyrus (PCG), where both, Aβ dense core plaques and Aβ diffuse deposits are seen. B: Both Aβ (T1-*i*) and rich hyperphosphorylated tau deposits (T1-*ii*) were present in the temporal cortex. Only scarce pathology was present in the primary sensory cortex (SC1-*i*, SC1-*ii*). Aβ plaques were the predominant pathology in the cingulate cortex (PCG-*i*) with only few hyperphoshporylated tau deposits (PCG-*ii*).
C: *In vitro* [F-18]FDDNP digital autoradiography of brain sections showing temporal lobe (E, F) revealed high tracer affinity for temporal lobe neocortical areas with mixed Aβ and

hyperphosphorylated tau IHC profiles and in hippocampus where only hyperphosphorylated tau IHC was detected.

Figure 4.
Co-localization analysis of FDDNP histofluorescence (A, D, G) and immunofluorescence (IF) for Aβ β-amyloid (B), neurofibrillary tangles (E) and α-synuclein (H) used for characterization of FDDNP labeled structures. Abundant dense-core and diffuse SP in striatum labeled with FDDNP (A) and closely matched with subsequent IF Aβdetection (B). The co-localization was quantified using superimposed images of both fluorescent signals (C). FDDNP labeling of neurofibrillary tangles in vitro (D) was confirmed by hyperphosphorylated tau IF detection (E, F). Lewy bodies (LB) displayed FDDNP fluorescence in subcortical structures and cortex (G, lb). They are smaller and scarcer in comparison with SP (G, sp). Alpha synuclein IF detection labeled LB (but not SP, H) and FDDNP fluorescent labeling of LB overlapped highly with red IF signal (I). Scale bar: A–C 100μm, D–F 50μm, G–I 40μm.
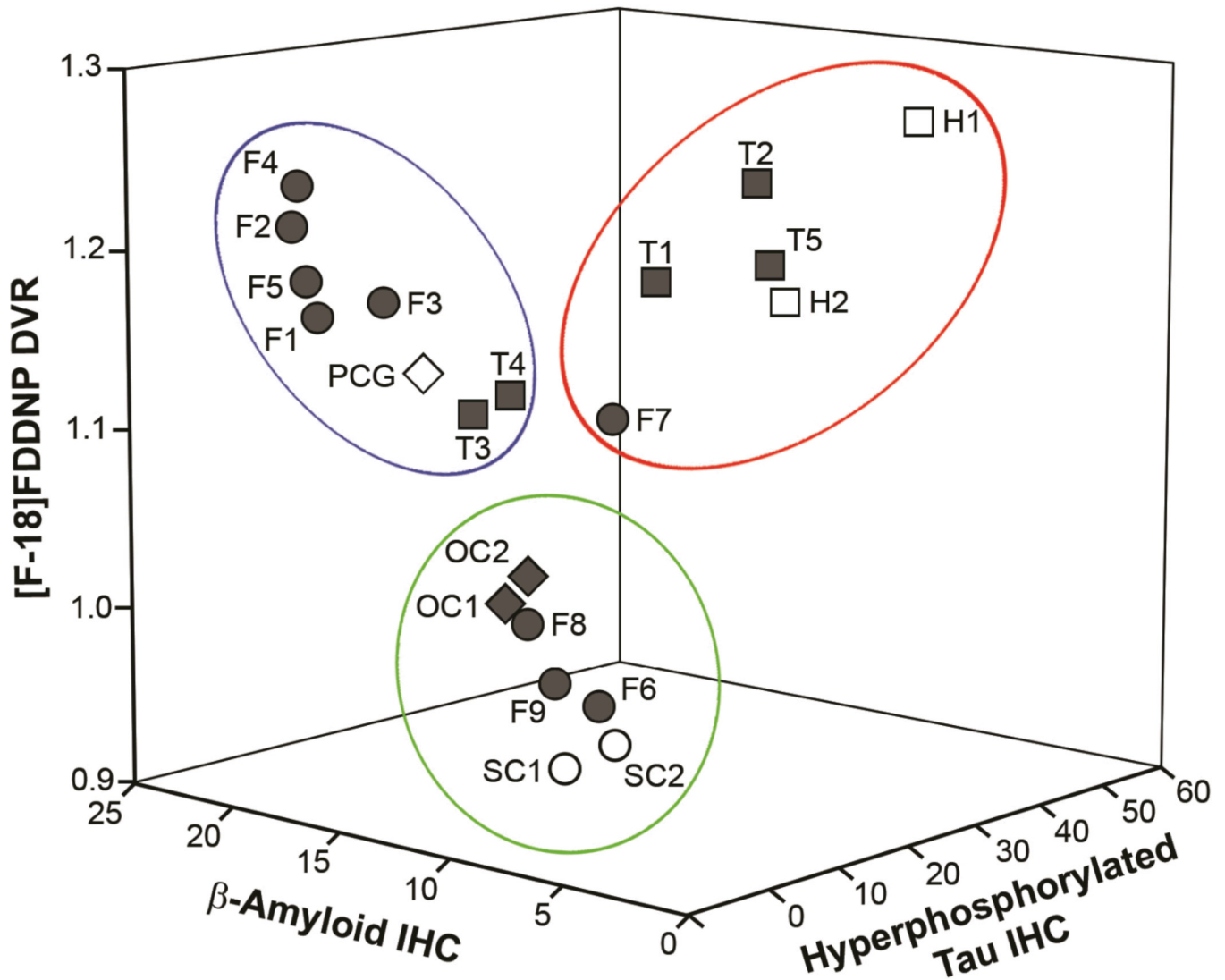
Figure 5.
3D scatter plot showing [F-18]FDDNP DVR values (axis z) as a function of Aβ IHC (axis x) and hyperphosphorylated tau IHC (axis y). Areas with high Aβ IHC load and low hyperphosphorylated tau IHC load are associated with high [F-18]FDDNP DVR values (blue oval) and so are areas with high hyperphosphorylated tau IHC load and low Aβ IHC load (red oval). This points to contribution of both types of pathologies to the *in vivo* [F-18]FDDNP signal. The names of ROIs are identical to those used in Table 1 and symbols are identical to those used in Figure 2. Regions with low levels of both IHC staining are grouped in the green oval.

Table 1

β-Amyloid and Tau immunohistochemistry "burden" values and [F-18]FDDNP DVR values for 21 regions of interest used for the analysis of this case.

	FDDNP DVR	Aβ IHC	Tau IHC
F1	1.160	20.80	3.52
F2	1.210	21.80	2.99
F3	1.170	18.90	7.00
F4	1.230	22.30	5.20
F5	1.177	22.00	5.50
F6	0.966	9.32	7.50
F7	1.104	13.27	21.90
F8	1.017	10.13	0.11
F9	0.986	9.07	0.55
PCG	1.137	16.40	5.03
OC1	1.025	11.34	0.70
OC2	1.043	10.23	0.50
T1	1.179	12.71	26.30
T2	1.230	11.31	36.40
T3	1.121	13.55	3.30
T4	1.124	14.32	10.60
T5	1.177	12.60	42.80
H1	1.260	8.55	51.48
H2	1.157	12.12	43.58
SC1	0.939	8.86	1.30
SC2	0.950	8.08	5.70

F: frontal; PCG: posterior cingulate gyrus; OC: occipital cortex; T: temporal cortex; H: hippocampus; SC: somatosensory cortex. IHC is expressed as percentage of tissue surface covered by IHC.

Table 2

Comparison of [F-18]FDG PET SUVR values for different brain regions of DLB subject with group values for control group showing globally decreased FDG utilization in this DLB subject.

	DLB	controls[†]	Z score
Global	1.465	2.011±0.086	−6.3
Frontal	1.497	2.120±0.096	−6.5
Parietal	1.264	2.017±0.140	−5.4
Lateral Temporal	1.411	1.930±0.147	−3.5
Medial temporal	1.522	1.571±0.105	−0.5
Posterior Cingulate	1.632	2.416±0.194	−4.0
Thalamus	1.903	2.211±0.105	−2.9
Striatum	2.227	2.317±0.099	−0.9
Motor	1.868	2.549±0.102	−6.6
Occipital	1.572	2.343±0.181	−4.3

All values are normalized to the cortical white matter. Z score signifies the difference between the DLB subject values and the mean values of the control group expressed in terms of SDs of the control group.

[†]Control group consists of 10 subjects (4F / 6M) aged 60.4±11.6 years (range 45–80 years).